

The simulation of high compressive stress and extrusion phenomenon for concrete face slabs in CFRDs under strong seismic loads

Jin Gong^{a,b}, Degao Zou^{a,b,*}, Xianjing Kong^{a,b}, Jingmao Liu^{a,b}, Kai Chen^{a,b}

^a The State Key Laboratory of Coastal and Offshore Engineering, Dalian University of Technology, Dalian, Liaoning, 116024, China

^b School of Hydraulic Engineering, Dalian University of Technology, Dalian, Liaoning, 116024, China

ARTICLE INFO

Keywords:

CFRD
High compressive stress: extrusion damage
SBFEM
Non-matching node

ABSTRACT

The evaluation of high compression zones for anti-seepage face slabs is an increasingly important task in the safety evaluation of high concrete faced rock-fill dams (CFRDs). This manuscript uses the scaled boundary finite element method (SBFEM) to construct a cross-scale model of the rockfill and bedrock in a high CFRD. Non-conforming elements are applied to independently refine the mesh locally in the concrete face slab, which allows an accurate modeling of the rotating and bending phenomenon experienced by the face slab zone. Meanwhile, the non-matching node interface is introduced to connect the locally refined face slab mesh to the rockfill zone and obtain the final cross-scale model for refined analysis. The generalized plastic constitutive model and a state-dependent elasto-plastic interface constitutive model are employed to capture the complex behaviors of rockfill and soil-structure interaction (SSI). Leveraging the above approaches, static and dynamic analyses of a high CFRD are conducted to identify high compressive stress zones and simulate the extrusion damage. The results indicate that self-weight, water pressure, friction force and seismic loads contribute to rotating and bending between face slabs, and can lead to significant local stress concentration within the surface of face slab near the longitudinal joints and may potentially extrusion damage.

1. Introduction

With the increasing development of renewable energy from hydro-electricity, the construction of high dams has gained worldwide attention. Particularly, the concrete faced rockfill dam (CFRD) is becoming an increasingly attractive type of dam due to its advantages in reliability, economy, and environmental adaptability. Many CFRDs have been built around the world, including the Barra Grande dam (in Brazil), the Zipingpu dam (in China), the La Yesca dam (in Mexico), the Bakun dam (in Malaysia), etc. With increased construction came modifications to the dam design. For example, heights of CFRDs are increasing from 200 m to 300 m, especially in China. Thus, the safety evaluation of such large-scale structures is of great significance for design and construction considerations [1–3].

Researchers have concluded that the potential failure of the anti-seepage structure, especially the concrete slab face, is a typical mode of damage in high CFRDs [4–6]. Thus, the refined analysis of concrete face slab in static and dynamic analysis is gradually becoming the core topic of numerical simulations for CFRDs [2,4,6]. Kong et al. [7–9] identified high stress zones within the face slab after impoundment,

during an earthquake, and after an earthquake. Zou et al. [10–13] proposed a refined way to perform static and dynamic analysis of concrete slab faces. Dakoulas et al. [14] and Xu et al. [4] used a plastic damage model for concrete to simulate stiffness degradation and strain softening and capture the response of face slabs during seismic excitation of 2D models. Arici [15] and Qu et al. [5] applied the cohesive zone model (CZM) to simulate the evaluation of crack performance.

Due to the weakness of concrete to tensile forces, much of the previous research [7–15] have focused on investigating the distribution of tensile stresses within the slab face. Conversely, when the compressive stress is excessive, CFRDs may experience extrusion damage. The high compressive stress zone of the face slab usually develops after impoundment or after an earthquake. Poorly compacted rockfill material is the main contributing reason for the development high compressive stress zone of face slab after impoundment [16,17]. However, with the improvement of rolling technology, CFRDs built in recent decades are mostly compacted adequately. Thus, most recently built CFRDs often do not experience extrusion damage of the face slab after impoundment. A great number of CFRDs with a height over 100 m are built in areas prone to earthquakes [2]. The compressive stress in the

* Corresponding author. The State Key Laboratory of Coastal and Offshore Engineering, Dalian University of Technology, Dalian, Liaoning, 116024, China.
E-mail address: zoudegao@dlut.edu.cn (D. Zou).

<https://doi.org/10.1016/j.soildyn.2021.106792>

Received 7 January 2021; Received in revised form 29 March 2021; Accepted 20 April 2021

Available online 29 May 2021

0267-7261/© 2021 Elsevier Ltd. All rights reserved.

axial direction of the face slab can accumulate rapidly under strong seismic loads, and may eventually lead to extrusion damage. The extrusion damage in the slab of the Zipingpu CFRD [1] during the Wenchuan earthquake is shown in Fig. 1. Thus, in this manuscript, the author focuses on studying the high compression zone of face slabs and simulate extrusion damage under seismic loads.

As seen in Fig. 1, extrusion damage and high compression zone typically occurs locally within the superficial zone of the face slab. Thus, a delicate mesh is needed only for areas that have the potential for extrusion damage. Thus, cross-scale modeling will be invaluable in generating practical 3D meshes for high CFRDs. Prior manuscripts have developed several approaches to perform cross-scale model [18,19]. In this paper, scaled boundary finite element method (SBFEM) [10,11,20,21] coupled with octree [22,23] is used in the rockfill and bedrock zones to generate the cross-model with high efficiency and autonomously. In addition, non-conforming elements [24–26] are introduced to replace the 8-nodes isoparametric elements to capture the bending and rotating behaviors within face slab. Non-matching node interfaces [12,13] have been used to connect the face slab and the cushion zone with flexible nodal distribution. Finally, the cross-scale model allows a rapid transition of element size from 0.4 m (high compressive zone in concrete face slab) to 20 m (bedrock zone). The implementation of cross-scale modeling can be found in section 3.

The application of advanced constitutive models is another vital issue in the modeling of CFRDs. In this paper, a generalized plasticity model [27,28] is applied to reflect the material properties of rockfill. A generalized plastic interface model [29,30] is employed to solve complex SSI problems.

This manuscript is organized as follows. Section 2 provides a brief introduction to the underlying theory. Section 3 details the modeling process along with the parameters of the material constitutive model and seismic loads. Section 4 evaluates the high compressive stress zone of face slab (with elastic model) under seismic load and investigates the effect of element size on the numerical behavior of the face slab. Section 5 explores a potential approach to mitigate the dynamic high compressive stress of the face slab. Finally, the plastic damage model is introduced to simulate the extrusion damage of face slab.

2. Introduction to numerical methods

All the numerical approach in this section have been verified with a numerical example or data measured in previous papers. The SBFEM is verified through the simulation of Koyna gravity dam and compared with data from a shake table test [11]. The non-matching node interface is applied to a metro structure and compared with results from the traditional FEM method [12]. The non-conforming element is adopted to simulate the cut-off wall with results from the traditional FEM method [31]. Through a combined use of the generalized plasticity model for rockfill and the generalized plastic interface model, the simulation of

Zipingpu CFRD is conducted and the results compared with measured data [1].

2.1. Scaled boundary finite element method

Song and Wolf [32] developed SBFEM, which is a semi-analytical method [33,34] that inherits the advantages of the finite element method (FEM) and the boundary element method (BEM). The ability of SBFEM to handle a complex geometries have allowed application towards a wide variety of modeling tasks [35–37]. Chen et al. [10,11,20,21] expanded the limits of SBFEM to enable analysis with nonlinear materials. In addition, the mean - value interpolation function [38] has been introduced to compute the displacement of each gauss point in each face. Through augmentation with octree [22,23], SBFEM can achieve cross-scale modeling in solid zones with high flexibility. The theory behind SBFEM is briefly introduced in the following, with more detail found in Refs. [10,11,20,21].

Through the mean - value interpolation function, the displacement within each face can be determined by:

$$\lambda_i(\mathbf{x}) = \frac{w_i(\mathbf{x})}{\sum_{j=1}^n w_j(\mathbf{x})} \quad (1)$$

$$w_i(\mathbf{x}) = \frac{\tan(\alpha_{i-1}/2) + \tan(\alpha_i/2)}{\|\mathbf{x} - \mathbf{v}_i\|} \quad (2)$$

where \mathbf{x} represents the coordinates of interpolation point, \mathbf{v}_i are the coordinate of the nodes. $\lambda_i(\mathbf{x})$ is the interpolating function, $w_i(\mathbf{x})$ is the mean - value weight function. α_i, α_{i-1} are the angle between interpolation point and nodes shown in Fig. 2. $\|\mathbf{x} - \mathbf{v}_i\|$ is the distance vector between interpolation point and nodes shown in Fig. 2.

According to the local coordinates (ξ, η, ζ) , the value of the shape

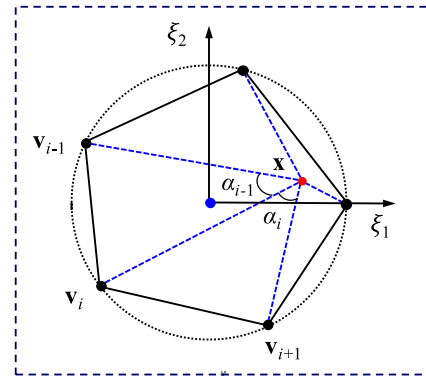


Fig. 2. Example of mean - value coordinates.



Fig. 1. Extrusion damage of face slab in post-earthquake Zipingpu CFRD.

function ϕ in each interpolation point can be obtained as follows:

$$\phi(\xi, \eta, \zeta) = N_u(\eta, \zeta) \psi_u \xi^{-(0.5+S_n)} \psi_u^{-1} \quad (3)$$

where (ξ, η, ζ) represents the local coordinates of the interpolation point, ϕ is the value of the shape function at each interpolation point. S_n is a diagonal matrix [10]. The matrix ψ_u comprises the nodal displacements, and its size depends on the degrees of freedom (DOF) elements. N_u is the polygonal shape function for a boundary surface.

$$B(\xi, \eta, \zeta) = \left[B_1(\eta, \zeta) \psi_u (S_n - 0.5) \xi^{-(1.5+S_n)} + \frac{1}{\xi} B_2(\eta, \zeta) \psi_u \xi^{-(0.5+S_n)} \right] \psi_u^{-1} \quad (4)$$

$$K_{ep} = \sum_{i=1}^{8m} B(\xi, \eta, \zeta)^T D_{ep}^i(\xi, \eta, \zeta) B(\xi, \eta, \zeta) V_i \quad (5)$$

$$[B] = \begin{bmatrix} \phi_{1,STRU} & 0 & 0 & \dots & \phi_{4,STRU} & 0 & 0 & -\phi_{1,SOIL} & 0 & 0 & \dots & -\phi_{n,SOIL} & 0 & 0 \\ 0 & \phi_{1,STRU} & 0 & \dots & 0 & \phi_{4,STRU} & 0 & 0 & -\phi_{1,SOIL} & 0 & 0 & \dots & -\phi_{n,SOIL} & 0 \\ 0 & 0 & \phi_{1,STRU} & \dots & 0 & 0 & \phi_{4,STRU} & 0 & -\phi_{1,SOIL} & 0 & 0 & \dots & -\phi_{n,SOIL} & 0 \end{bmatrix} \quad (11)$$

where B_1 and B_2 are transition matrices [2], B , K_{ep} , and D_{ep} represent the strain displacement transformation matrix, stiffness matrix and constitutive model matrix, respectively. The diagonal entries of S_n are composed of the real parts of the eigenvalues. The entries include two zeros (representing the two modes of translational rigid body motion) and negative numbers.

2.2. Modeling interfaces with non-matching nodes

Using the 8-node interface element (4 nodes for 2D elements) and meshless method [39–41] as the foundation, Gong et al. [12,13] developed the non-matching node interface to simulate soil-structure interaction. On the structural side, four nodes in each element are used for linear interpolation. A set of nodes within the supporting area [12,13] on side of the soil is used for RBF [42–45] interpolation. Thus, the approach accomplishes cross-scale modeling between the concrete slab face and cushion zone with flexible nodal distribution on either side of the interface. In addition, the most interface constitutive models can be directly employed in this cross-scale modeling approach, thereby significantly enriching the potential applications of non-matching node interfaces in geotechnical engineering. The remainder of this section summarizes the derivation of the above method, and more details found in Refs. [12,13].

To compute the displacement along the structural side, the following equations can be adopted.

$$u_{STRU}(x) = \phi_{1,STRU} u_1 + \phi_{2,STRU} u_2 + \phi_{3,STRU} u_3 + \phi_{4,STRU} u_4 \quad (6)$$

$$\begin{aligned} \phi_{1,STRU} &= \frac{1}{4} \left(1 - \frac{x}{L_x} \right) \left(1 - \frac{y}{L_y} \right) & \phi_{2,STRU} &= \frac{1}{4} \left(1 - \frac{x}{L_x} \right) \left(1 + \frac{y}{L_y} \right) \\ \phi_{3,STRU} &= \frac{1}{4} \left(1 + \frac{x}{L_x} \right) \left(1 - \frac{y}{L_y} \right) & \phi_{4,STRU} &= \frac{1}{4} \left(1 + \frac{x}{L_x} \right) \left(1 + \frac{y}{L_y} \right) \end{aligned} \quad (7)$$

$$u_{SOIL}(x) = \sum_{i=1}^n B(r_{ij}) a_i + \sum_{k=1}^m p(l_k) b_k \quad (8)$$

$$B(r_{ij}) = (r_{ij}^2 + C^2)^q \quad (9)$$

where x and y represent the coordinates of the interpolation point in local coordinates. L_x and L_y are the lengths of the element in the normal and tangential directions on the structural side. u_{STRU} and u_{SOIL} are the displacements along the structural and soil side. ϕ is the shape function

of corresponding nodes on the structural side. $B(r_{ij})$ is a multi-quadric (MQ) radial basis where C , q are two constant parameters. r_{ij} refers to the distance between node i and node j within the supporting domain. In addition, $p(l_k)$ refers to the added basis of the MQ radial basis. a_b , b_k are the constants to be computed for the MQ radial basis [13].

$$\Delta u = u_{STRU}(x) - u_{SOIL}(x) = \left\{ \phi_{1,STRU} \quad \dots \quad \phi_{4,STRU} \right\} \begin{Bmatrix} u_{1,STRU} \\ \dots \\ u_{n,STRU} \end{Bmatrix} - \left\{ \phi_{1,SOIL} \quad \phi_{2,SOIL} \quad \dots \quad \phi_{n,SOIL} \right\} \begin{Bmatrix} u_{1,SOIL} \\ u_{2,SOIL} \\ \dots \\ u_{n,SOIL} \end{Bmatrix} \quad (10)$$

The differential matrix B of each gauss point is computed with equation (11). Note that B is a $3 \times (3 \times (4 + n))$ matrix in 3D problems.

Finally, through the gaussian integration, the stiffness matrix K of the non-matching node interface is obtained as follows:

$$[K]' = \int_A [B]^T [D] [B] dA \quad (12)$$

where D represents the constitutive model matrix.

2.3. Non-conforming element

The interpolation function in isoparametric elements is linear, and may be inadequate for simulating bending and rotations within the face slab. To solve the above issue, non-conforming elements [24–26] are introduced to replace the more traditional 8-node isoparametric elements in the face slab. Through adding an internal quadratic basis for the displacement field, the interpolation function of non-conforming elements can satisfy the complete quadratic basis at each gauss position without the need for additional nodes. The process of derivation is shown in the following with more detail found in Refs. [24–26].

The displacement field of Wilson non-conforming elements can be obtained by:

$$u = N\delta + N_a\delta_a \quad (13)$$

$$N = \begin{bmatrix} N_1 & 0 & 0 & \dots & N_8 & 0 & 0 \\ 0 & N_1 & 0 & \dots & 0 & N_8 & 0 \\ 0 & 0 & N_1 & \dots & 0 & 0 & N_8 \end{bmatrix} \quad (14)$$

$$N_a = \begin{bmatrix} N_{a1} & 0 & 0 & N_{a2} & 0 & 0 & N_{a3} & 0 & 0 \\ 0 & N_{a1} & 0 & 0 & N_{a2} & 0 & 0 & N_{a3} & 0 \\ 0 & 0 & N_{a1} & 0 & 0 & N_{a2} & 0 & 0 & N_{a3} \end{bmatrix} \quad (15)$$

where $N_i = \frac{1}{8}(1 + \xi\xi_i)(1 + \eta\eta_i)(1 + \zeta\zeta_i)$ $N_{a1} = 1 - \xi^2$ $N_{a2} = 1 - \eta^2$ $N_{a3} = 1 - \zeta^2$

Through the complete linear and quadratic bases, the strain can be derived:

$$\epsilon = B\delta + B_a\delta_a \quad (16)$$

where N and N_a respectively represent the matrix of the shape function on each node and the internal additional shape function, B and B_a are respectively the strain matrix and internal additional strain matrix. Similarly, δ and δ_a are the displacement of each nodes and internal additional displacement [24].

$$\begin{bmatrix} \mathbf{K}_{uu} & \mathbf{K}_{ua} \\ \mathbf{K}_{au} & \mathbf{K}_{aa} \end{bmatrix} \begin{bmatrix} \delta \\ \delta_a \end{bmatrix} = \begin{bmatrix} \mathbf{P}_u \\ \mathbf{P}_a \end{bmatrix} \quad (17)$$

where P and P_a are the external force vector and an additional external force vector [4]. The K matrices are described as follows:

$$\mathbf{K}_{uu} = \int_V B^T DB dV \quad \mathbf{K}_{ua} = \int_V B^T DB_a dV \quad \mathbf{K}_{au} = \int_V B_a^T DB dV \quad \mathbf{K}_{aa} = \int_V B_a^T DB_a dV \quad (18)$$

2.4. Generalized plasticity model for rockfill

An improved version of the generalized plastic constitutive equations presented by Zienkiewicz and Pastor [27,28] can be used to better capture model behavior under cyclic hysteresis and stress correlation. The above modified model unifies parameters for static analysis, dynamic analysis, plastic deformations and has been successfully applied in several geotechnical structures. The abridged theory is provided in the following paragraphs and further details can be found in Refs. [27, 28].

Firstly, the relationship between stress and dilatancy can be expressed as:

$$d\varepsilon_v^p = \frac{d\varepsilon_v^p}{d\varepsilon_s^p} = (1 + \alpha_g)(M_g - \eta) \quad (19)$$

where $d\varepsilon_v^p$ and $d\varepsilon_s^p$ are the incremental plastic volumetric and deviatoric strains, respectively, M_g is the slope of the critical state line in the $p-q$ plane, $\eta = q/p$ is the stress ratio, and α_g is a model parameter.

$$M_g = \frac{6 \sin \phi'_g}{3 + \sin \phi'_g \sin 3\theta} \quad (20)$$

In the elastic stage, the behavior is described with shear and bulk moduli:

$$G = G_0 p_a (p/p_a)^{m_s} \quad (21)$$

$$K = K_0 p_a (p/p_a)^{m_v} \quad (22)$$

where G_0 , K_0 , m_s , and m_v are parameters for elastic modulus parameters.

On the other hand, the plastic modulus under loading H_L and unloading H_u can be defined respectively as:

$$H_L = H_0 \cdot p_a \cdot (p/p_a)^{m_l} \cdot H_f \cdot (H_v + H_s) \cdot H_{DM} \cdot H_{den} \quad (23)$$

$$H_u = \begin{cases} H_{u0} p_a (p/p_a)^{m_u} (\eta_u/M_g)^{-\gamma_u} & |\eta_u/M_g| < 1 \\ H_{u0} & |\eta_u/M_g| \geq 1 \end{cases} \quad (24)$$

where H_0 is the plastic modulus number; H_f , H_v , and H_s are plastic coefficients; H_{den} , H_{DM} are the densification coefficient; p_a is the atmospheric pressure; exponents m_l and m_u are obtained by fitting the whole stress-strain curve under different confining pressures [28].

2.5. Generalized plastic interface model

As for the interface zone, Liu et al. proposed an elasto-plastic constitutive model that considers state-dependence in three dimensions based on the generalized plasticity framework [29,30]. This model can accurately capture the complex behaviors within the interface zone, including shear dilation, shear contraction, stress hardening, softening and particle breakage. The interface model is briefly described

below and more details can be found in Refs. [29,30].

The elastic matrix is described as:

$$\mathbf{D}^e = \begin{bmatrix} D_s & & \\ & D_s & \\ & & D_n \end{bmatrix} \quad (25)$$

On the other hand, the plastic modulus is calculated by:

$$H = H_0 \frac{1}{1 + \psi} \left(\frac{\sigma_n}{p_a} \right) \left(1 - \frac{\rho}{\rho_p} \right) (1 + \rho)^{-2} f \quad (26)$$

where f represents a maximum stress surface defined in τ - σ_n stress space.

$$f = \tau - M \sigma_n \left(\frac{\alpha}{\alpha - 1} \right) \left[1 - \left(\frac{\sigma_n}{\sigma_c} \right)^{\alpha - 1} \right] = 0 \quad (27)$$

where α and M are model constants [29].

$$\psi = e - e_c \quad (28)$$

where e is the void ratio and e_c is critical void ratio.

The direction of the plastic flow and the loading direction vector n is expressed as

$$\mathbf{n} = (n_x, n_y, n_n)^T \quad n_x = \frac{\tau_x}{\tau \sqrt{d_f^2 + 1}} \quad n_y = \frac{\tau_y}{\tau \sqrt{d_f^2 + 1}} \quad n_n = \frac{d_f}{\sqrt{d_f^2 + 1}} \quad (29)$$

$$d_f = r_d \alpha \left((M_f + k_m \psi) \sqrt{\rho_{\max}/\rho} - \eta \right) \exp(c_0 / \eta) \quad (30)$$

where α , r_d , and k_m are introduced for simulating dilatancy, M_f indicates the loading flow direction, η is the stress ratio in the $p-q$ plane, and ρ and ρ_{\max} are described in Fig. 3 as follows:

Finally, the criteria of loading or unloading can be defined as.

Loading: $\mathbf{n} : d\boldsymbol{\sigma}^e > 0$

Unloading: $\mathbf{n} : d\boldsymbol{\sigma}^e < 0$ (31)

Neutral loading: $\mathbf{n} : d\boldsymbol{\sigma}^e = 0$

3. Modeling and simulation parameters

3.1. Geometric modeling

In this manuscript, a 3D CFRD with 240 m height is introduced to numerically evaluate the high compressive stress zone under strong seismic loads. The geometrical model is shown in Fig. 4. We defined the x direction as the direction along the river, the y direction as the vertical direction and z direction as the dam axial direction. The dam has upstream and downstream slopes of 1:1.4 and 1:1.6, respectively, and both banks of the river valley share a 1:1 slope. The width is 80 m at the bottom of the valley. To capture the dam-foundation dynamic

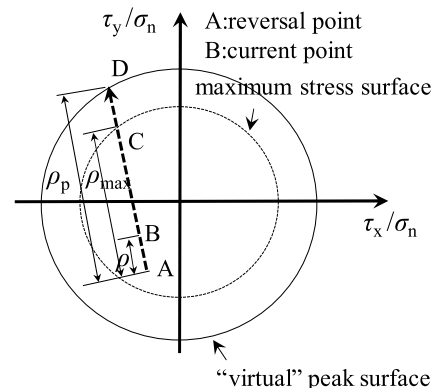


Fig. 3. Illustration of ρ and ρ_{\max} .

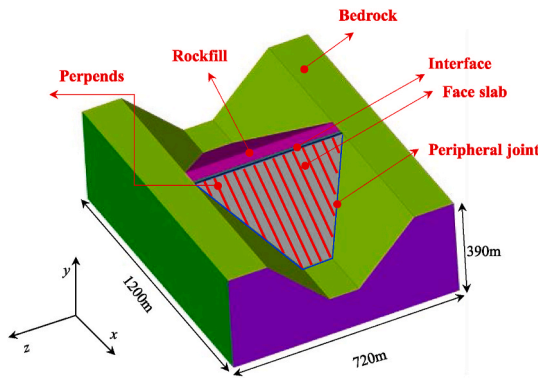


Fig. 4. The geometry model of 3D CFRD.

interaction, the interfacing length for the foundation in the model is about $1.0 H$ (H for dam height) following previous research [1,29]. The thickness of the anti-seepage concrete face slab increases according to $0.3 + 0.0035 h$, where h is the depth from the water surface. In engineering practice, the face slab has steel reinforcement in two directions. However, the rebar is applied to bear the tensile stress instead of compressive stress. Meanwhile, it presents significant difficulties in modeling 3D CFRDs considered the rebar. Thus, the steel reinforcement concrete face slab is not considered in this simulation.

Differences over several orders of magnitudes exist between the elements composing the face slab and rockfill, bedrock zone. Thus, to balance computational efficiency and precision, the cross-scale model is necessary. Meanwhile, the potential high compression stresses zone for the face slab lies within the center of the valley and a locally refined mesh is needed for modeling such an area. Such a requirement can be achieved by independent modeling between the face slab, the rockfill, and the bedrock. In answer to the above challenges, this section presents an effective way to achieve cross-scale modeling and local mesh refinement as follows (see also Figs. 5–7):

Step 1. A cross-scale model (elements size from 2 m to 20 m) for the rockfill and bedrock is constructed with 298,145 elements. Several complex elements (polyhedrons elements) are also introduced through automatic meshing, which cannot be solved without coupled SBFEM-FEM.

Step 2. The mesh of face slab is independently established with 1 m meshes along the axial direction and 2 m meshes along the vertical direction. As the high compression zone is located in the center of the valley [7–9], the meshes in these area is further refined with 0.4 m

meshes along the axial direction of the dam. The face slab is divided into a select number of layers (i.e. 5 layers in this manuscript) along the direction of the thickness. Meanwhile, non-conforming elements are introduced to replace the 8-node interface elements. Finally, 243,165 elements are used to model the face slab.

Step 3. The non-matching node interface is introduced to connect differently sized meshes between the face slab, the rock-fill, and the bedrock. The specialized interface captures the complex soil-structure interaction with elastic-plasticity interface constitutive equations. Joint elements are used to simulate vertical joints on the concrete face slab (20 m between vertical joints). The vertical joints have a significant influence for the stress distribution along the axial direction of the dam. Viscoelastic artificial boundaries are used for dynamic analysis. The final meshes are shown in Fig. 5 with 645,892 elements and 754,213 nodes.

3.2. Parameters used for static and dynamic analyses

The 240 m CFRD model is constructed in 30 steps. Sixty steps are dedicated to simulating the impoundment process (water level of 180 m) before an earthquake. Table 1 lists the material parameters used by the generalized plastic model to describe the rock-fill, cushion and transition zones [28]. The state-dependent elastic-plastic interface constitutive model (Table 2) is employed to simulate the soil-structure interaction. The linear elastic model is used for concrete face slab and bedrock (Table 3) [29]. The asphalt board [46] is considered as filling materials for the vertical joints (i.e. hard joints) (Table 4). It should be noted that in this manuscript, all vertical joints are simulated with interface elements, and the width of vertical joints is 10 mm in the following simulation.

Compaction parameters and filling density		
E	$\rho/\text{kg/m}^3$	D_r
0.231	2210	93.8%
0.157	2350	94.8%
0.188	2290	94.6%

Material properties remain the same for both dynamic and static analysis. The input ground motion uses a simulated earthquake wave specified by the “Specifications for seismic design of hydraulic structures”. The input seismic load is a 20 s wave with peak ground acceleration (PGA) of 0.497 g in the horizontal direction x , and 0.334 g in both the vertical direction y and dam axial direction z as shown in Fig. 8. The response spectrum of the seismic wave are shown in Fig. 9.

The above seismic loads are applied through the viscoelastic

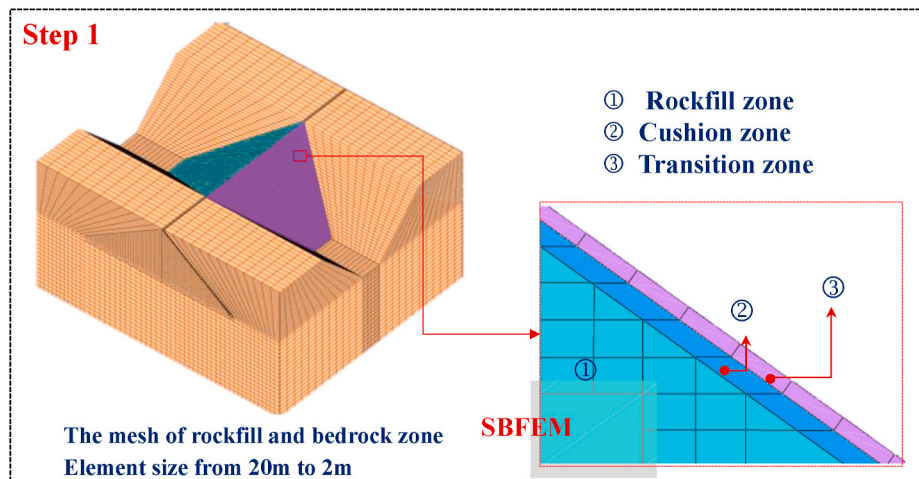


Fig. 5. The process of CFRD modeling: Step 1. Overview of the different zones. Note the difference in element density across different zones.

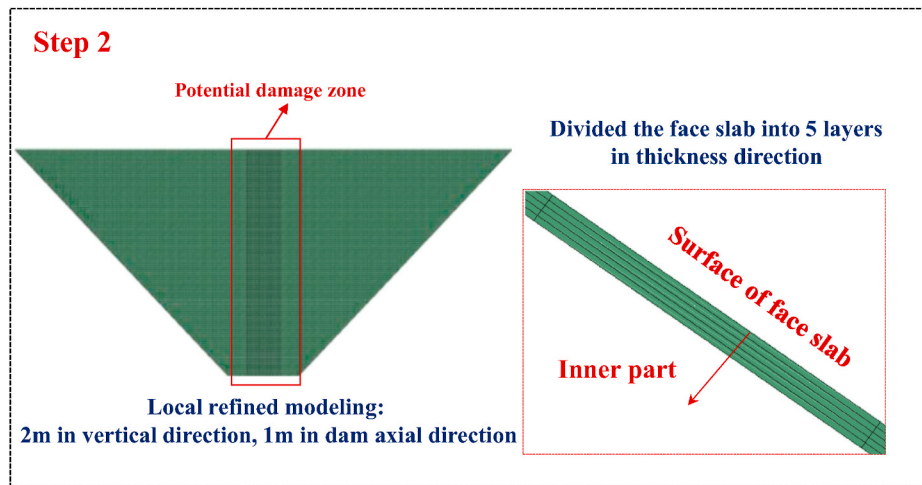


Fig. 6. The process of CFRD modeling: Step 2. The high compressive stress zone in the face slab is locally refined.

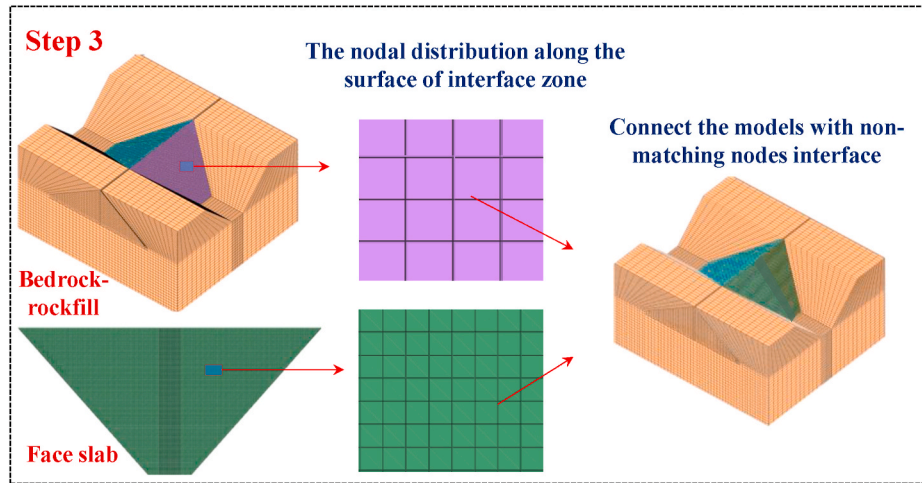


Fig. 7. The process of CFRD modeling: Step 3. Introducing the non-matching node interface between differently sized meshes.

Table 1

The material parameters for the rockfill, cushion and transition zones [28].

	Elastic modulus				Plastic loading direction				Plastic modulus								
	G_0	K_0	m_s	m_v	M_g	M_f	α_f	α_g	m_l	m_u	r_d	γ_{DM}	γ_u	β_0	β_1	H_0	H_{U0}
Rockfill	1000	1400	0.5	0.5	1.8	1.38	0.45	0.4	0.2	0.2	180	50	4	35	0.022	1800	3000
Cushion	980	1290	0.5	0.55	1.6	1.38	0.35	0.4	0.2	0.2	150	20	4	30	0.025	1500	2800
Transition	980	1290	0.55	0.55	1.6	1.38	0.3	0.4	0.2	0.2	120	20	4	25	0.03	1500	2800

Table 2

The material parameters for the interface between cushion zone and face slab [29].

Elastic modulus		Critical state			Particle breakage			Plastic direction		Loading direction		Plastic modulus		
D_{s0}/kPa	D_{n0}/kPa	M_c	$e_{\tau 0}$	Λ	$a/\text{kPa}^{0.5}$	b	C	α	r_d	k_m	M_f	k	H_0/kPa	f_h
1000	1500	0.88	0.4	0.091	224	0.06	3.0	0.65	0.2	0.6	0.65	0.5	8500	2

Table 3

The material parameters for the face slab and bedrock.

Component	E/GPa	$\rho/\text{kg}\cdot\text{m}^{-3}$	ν
Face slab	31	2500	0.17
Bedrock zone	10	2400	0.25

Table 4

The material parameters for the asphalt board as the filling materials for vertical joints [46].

Component	E_t/Pa	E_c/Pa	E_b/Pa
Asphalt board	1×10^6	1×10^{10}	2×10^5

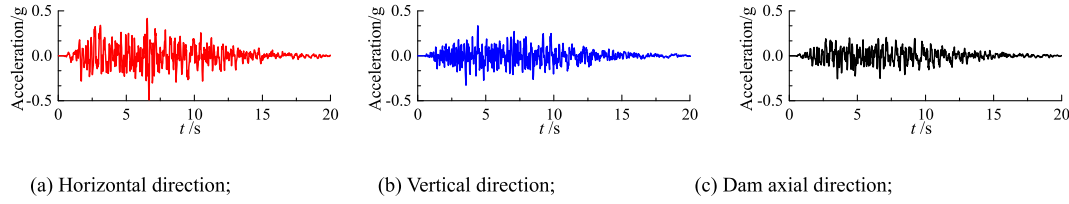


Fig. 8. Time history of the acceleration during earthquake along different directions.

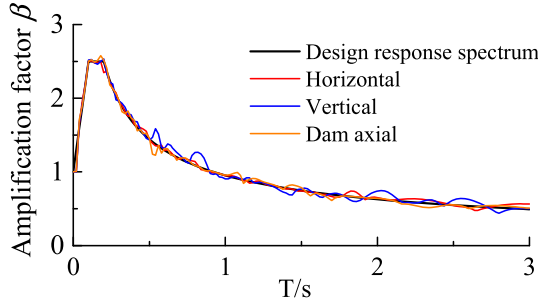


Fig. 9. The acceleration amplification response spectrum.

boundary and equivalent load [47]. Viscoelastic boundary elements are introduced at the boundary of the bedrock. The equivalent load can be simulated with equation (32) as follows:

$$\mathbf{F}_b = \mathbf{R}_b^{ef} + \mathbf{C}_b \dot{\mathbf{u}}_b^{ef} + \mathbf{K}_b \mathbf{u}_b^{ef} \quad (32)$$

where \mathbf{u}_b^{ef} , $\dot{\mathbf{u}}_b^{ef}$ and \mathbf{R}_b^{ef} are, respectively the displacement vector, velocity vector and the corresponding force vector induced at the system boundary nodes by the free wave field, and \mathbf{K}_b and \mathbf{C}_b are the additional stiffness matrix and damping matrix of the viscoelastic boundary element, respectively.

The dynamic analysis uses the Newmark- β [48] method and increments in steps of 0.01s during integration until 1% convergence is reached. Meanwhile, Rayleigh damping [49] is chosen as a gauge for damping characteristics shown in Fig. 10.

The damping matrix [C] is related to the viscous coefficient of the material. The damping matrix can be expressed as follows:

$$[C] = \alpha[M] + \beta[K] \quad (33)$$

where α and β are both damping coefficients. Yoshida et al. [49] proposed that the minimum damping ratio can be expressed as

$$h_{\min} = \sqrt{\alpha\beta} \quad (34)$$

Then, a sensitive frequency range f_a and f_b needs to be defined. In geotechnical engineering, this range is typically between 0.5 and 5 Hz. The damping ratio at the boundary can be expressed as

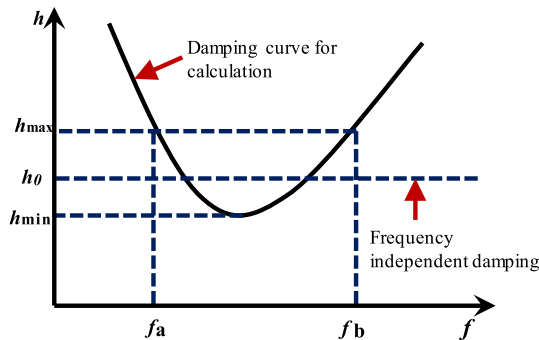


Fig. 10. The relation between damping ratio and frequency (Yoshida 2002).

$$h_{\max} = \alpha/2w_b + \beta w_b/2 \quad (35)$$

$$h_{\max} = \alpha/2w_a + \beta w_a/2 \quad (36)$$

where $w = 2\pi f$, the frequency-dependent damping can be expressed by:

$$h_0 = (h_{\min} + h_{\max})/2 \quad (37)$$

Through the above equations, the damping coefficients α and β can be estimated. When the damping ratio $h < h_0$, then $h = h_0$. The relation between damping ratio and frequency is shown in Fig. 5. In this paper, the $f_a = 0.5$, $f_b = 3$. The frequency independent damping is $h_0 = 5\%$ for the face slab, $h_0 = 2\%$ for the rockfill and $h_0 = 1\%$ for the canyon rock material [50].

4. Numerical results

4.1. Evaluation of high compressive stress

An initial static analysis is conducted using the model and parameters described in the prior sections Fig. 11 shows the deformation of rockfill zone (the maximum cross-section) from the effect of self-weight and post-impoundment water pressure.

With the rising of water level, the rockfill horizontally displaced from the upstream side to downstream side. Due to the dual sided restriction imposed by the river valley, the concrete face slab deforms with the rockfill, thereby further contributing to the deflection towards the downstream direction (Fig. 12). The maximum displacement is located at the lower middle part of the face slab, and is similar with the location of maximum incremental horizontal displacement in the rockfill. The relative thinness of the face slab results in bending and rotating along the slope. Accordingly, rotation may occur near the vertical joints between different parts of the face slab, where the angle between the rotating parts of the face slab is α .

The rotation can generate stress concentration on the surface of face slab. Fig. 13 shows the angle of rotation as the water level increased. The difference in compressive stresses after impoundment along dam axial direction within the surface and along the innermost layer of face slab is shown in Fig. 14.

The above results indicate that the maximum compressive stress occurs at $0.4H$ of the face slab. Both the surface and inner parts of face slab are compressed, however a significant difference in the stress levels between the two parts is present due to the small rotation. Though stress is concentrated within the surface of face slab, the maximum compressive stress along the axial direction of the dam is far from the compressive strength of concrete. Thus, extrusion damage does not occur in the above static analysis in this simulation. On the other hand, the tensile stresses are significantly increased within the innermost layer of the face slab (i.e. edge of face slab), which may lead to other potential problems (e.g. excessive opening of the peripheral joint), but that are outside the scope of this study.

The dynamic analysis builds upon the static analysis and utilizes the same model and set of parameters. Firstly, the post-earthquake deformation of the rockfill zone (the maximum cross-section) is obtained as shown in Fig. 15. Under the effect of water pressure and seismic load, the maximum post-earthquake deformation occurred at the top of the

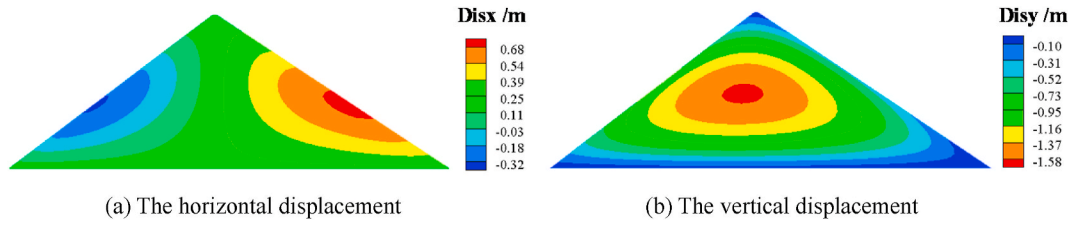


Fig. 11. The deformation of rockfill zone after impoundment.

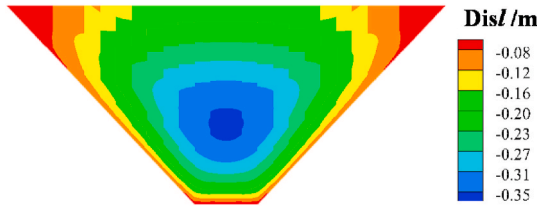


Fig. 12. The deflection of face slab after impoundment.

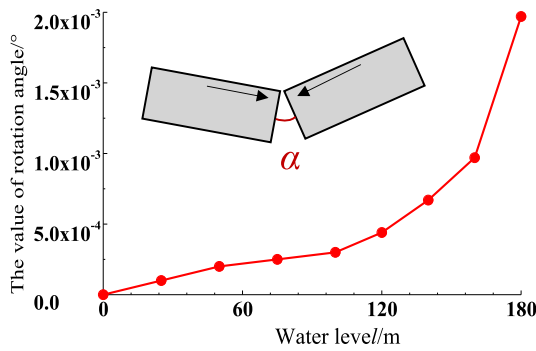


Fig. 13. The value of rotating angle with water level.

rockfill zone. Meanwhile, due to the friction between the cushion zone and the face slab, the maximum post-earthquake deflection also occurred at the top of face slab.

Due to the width of face slab at the top position, the restriction from the bedrock at both sides are relatively weak. Thus, the position of the maximum compressive zone on the face slab moves down along the dam direction to about $0.85H$. Meanwhile, the restriction points towards the middle part of face slab. Thus, the relatively high compressive zone lies in the middle of the river valley and about $0.85H$ height of face slab. A previous study by Kong et al. [7] presented a similar distribution of the high compressive stress zone on the face slab. Fig. 16 shows the post-earthquake deformation characteristics of the face slab.

Within the high compressive stress zone, the relative thinness of the face slab results in bending and rotating. Due to the existence of pre-pends, a different part of face slab may rotate along the axis of vertical joints shown in Fig. 16. According to the above discussion, the maximum angle of rotation occurs in the middle of river valley along vertical joint. Through a sub-model of the face slab-interface-cushion zone, Zhou et al. [17] also concluded that the rotation extrusion damage may occur within the face slab. The rotation along the pre-pends can generate stress concentrations on the surface of the face slab, which leads to a significant rising of compressive stress along the dam axial direction within the outermost layer face slab. Xu et al. [16] and Zhou et al. [51] also pointed out that the stress concentration phenomenon should be avoided to reduce the high compressive stress of the face slab.

Fig. 17 compares the post-earthquake compressive stresses within the surface and inner parts of the face slab in the axial direction of the dam. The figure shows that the maximum post-earthquake stress occurs

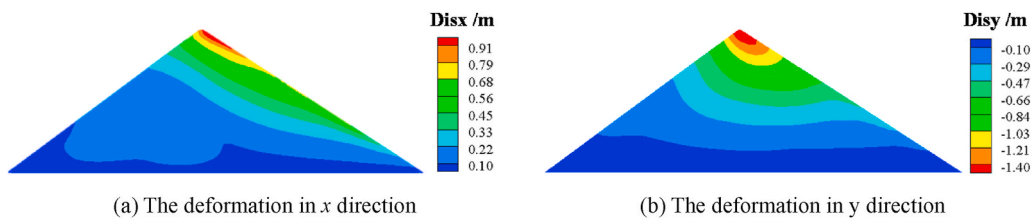


Fig. 14. Comparison of compressive stresses in face slab along the axial direction of the dam (negative for compression).

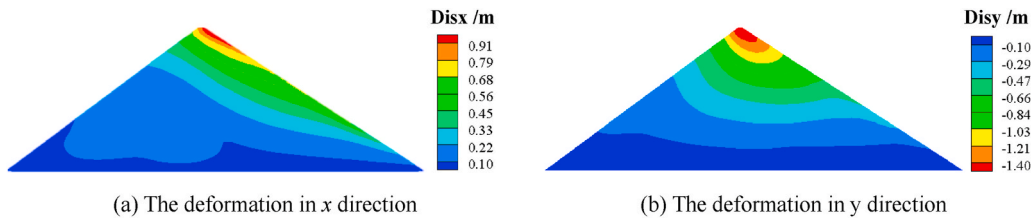


Fig. 15. Post-earthquake deformation in the maximum cross-section of rock-fill.

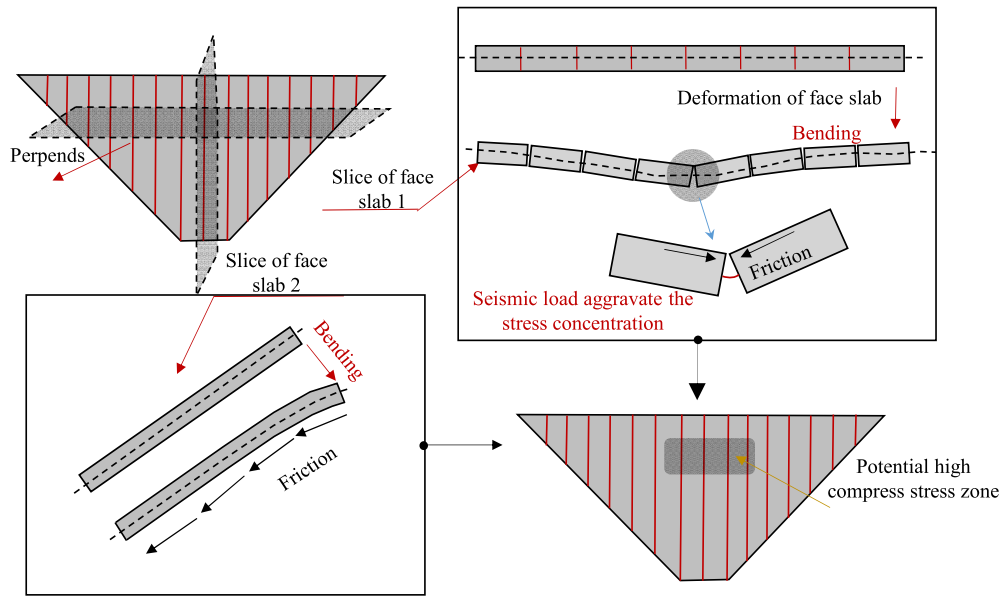


Fig. 16. The post-earthquake deformation characters of face slab.

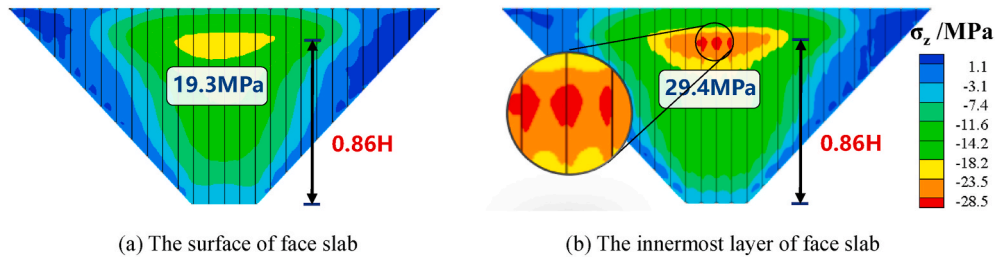


Fig. 17. The comparison of compress stress in dam axial direction in face slab (negative for compression).

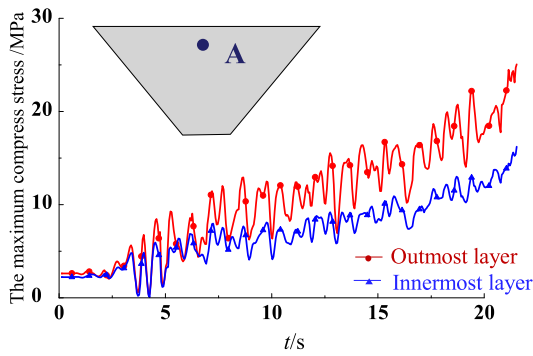


Fig. 18. Stress vs seismic time history.

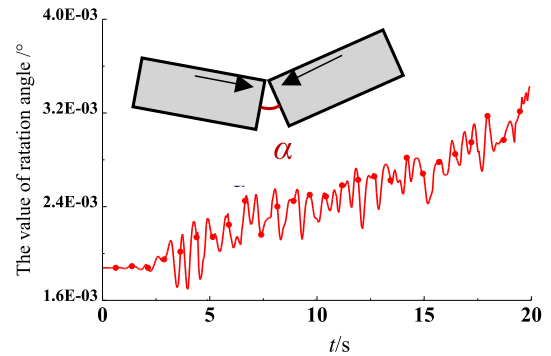


Fig. 19. Rotation angle vs seismic time history.

at 0.86H and high compressive stress zone locates near the vertical joints. The time history of the maximum stresses and the degree of rotation along the slope is shown in Fig. 18 and Fig. 19, respectively. The compressive stress oscillates and accumulates in both the surface and innermost layer of the face slab shows during the earthquake.

The seismic excitation caused further deformation at the top of the rockfill, thereby increasing the degree of rotation between face slabs along the slope and amplifying the stress concentration in the surface of concrete face slab. The maximum compressive stress reached 29.4 MPa in the middle of valley located near the vertical joints at 0.86H. For reference, the uniaxial compression strength of C30 concrete is 27.8 MPa, which indicates that the extrusion damage may occur at the surface of face slab after earthquake.

4.2. Effect of face slab meshing

The effect of the face slab meshing on results is investigated in this section to help select the appropriate mesh size in concrete face slab. Firstly, the face slab is divided between 1 and 6 layers in the normal direction. The thickness of elements varies from 0.3 m to 0.05 m at the top of the face slab. The compressive stresses along the axial direction of the dam for the innermost and outermost layers of face slab is shown in Fig. 20. The results suggests that only multi-layer (5 layers for this simulation) elements can effectively model the bending, rotation between face slabs and the stress concentrations, all of which contribute to

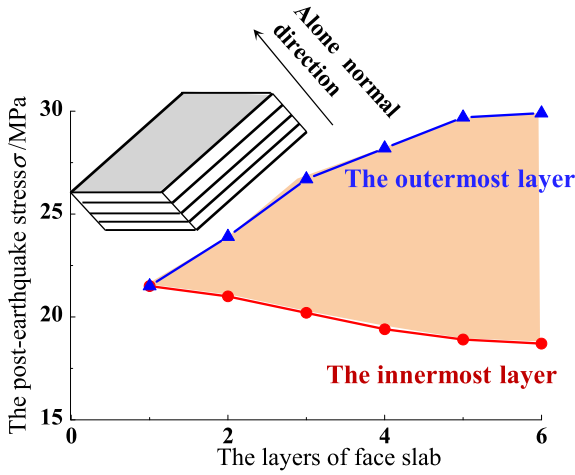


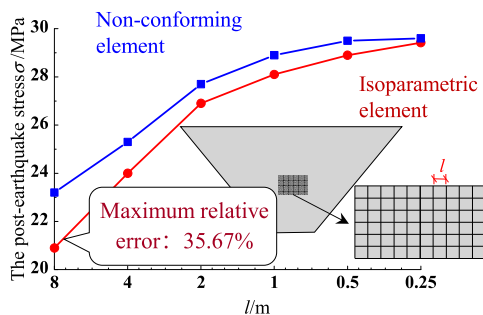
Fig. 20. The size effect analysis of face slab in normal direction.

high compressive stress.

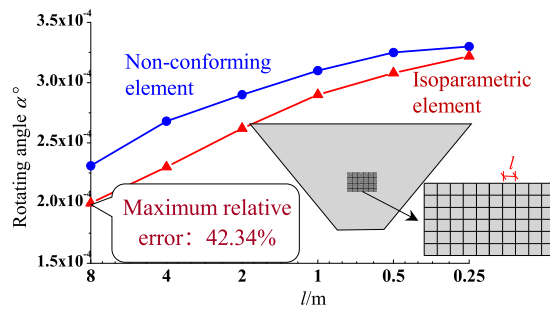
Therefore, the face slab consisted of 5 layers of elements in the normal direction, and the minimum thickness of the face slab is 0.06 m. The precision of elements decreases if the size of the other two directions (axial, slope directions) are too large by comparison. Thus, the size analysis for face slab within the high compressive stress zone covers 8 m–0.25 m meshes in the axial direction. Meanwhile, in order to simulate the bending and rotation between face slabs, the non-conforming element is also considered as shown in Fig. 21. Compared with the 8-node element, the non-conforming element offers higher precision in evaluating the high compressive stress zone. With the non-conforming element, the precision can be guaranteed where the mesh size reaches 0.5 m along the axial direction of the dam.

In this example, the effect of the face slab meshing along the direction of the slope is shown in Fig. 22 for sizes 5.6 m to 0.7 m. The error, which uses the 0.7 m results as the reference, is listed in Table 5. The results suggest that the element size along direction of the slope has little influence when the size reaches 2.8 m. Thus the following work uses the size of 2.8 m for face slab element along the direction of the slope to strike a balance element population and numerical precision.

The above results show that a locally delicate mesh for the face slab is necessary for adequately evaluating the high compressive stress. However, the large number of elements needed for implementing a delicate mesh can be computationally expensive and have impeded prior related research efforts. This manuscript therefore turns to cross-scale modeling to balance precision and efficiency. Particularly, a combination of non-matching node interface, SBFEM and non-conforming elements serve as the core tools for properly evaluating the high compressive stress zone in 3D CFRDs.



(a) The maximum stress with different meshes



(b) The maximum rotation angle with different meshes

Fig. 21. The size effect analysis for face slab along the axial direction.

4.3. Approaches to reducing the high compressive stress

The analyses conducted in the preceding sections point towards the deformation of the rockfill as the primary cause of high compressive stress. Therefore, any measures that can effectively control the deformation of the dam body [7–9], such as decreasing the water level, replacing the material in the rockfill area, etc., will help mitigate high compressive stress. However, the details of such approaches are beyond the scope of this manuscript.

(1) Replacing hard joints with soft materials

The material of longitudinal joint can greatly influence the compressive stresses of the face slab, especially along the axial direction of the dam [52]. Compared with hard joints made of asphalt boards ($E_{nc} = 1 \times 10^{10} \text{ Pa}$), the soft filler used in the vertical joints can effectively mitigate high compressive stress [53,54]. Thus, this section utilizes two soft filler materials for the longitudinal joint and subjects the CFRD model (water level 210 m, bottom valley width 80 m, PGA 0.6 g) to verify improvements in high compressive stress. The results (only the relative high stress zone) are shown in Fig. 23. In case (a), the hard joint with asphalt is introduced for comparison. In case (b), birch ($E_{nc} = 2.3 \times 10^8 \text{ Pa}$) is used as the filler material for longitudinal joints. In case (c), rubber ($E_{nc0} = 5 \times 10^6 \text{ Pa}$, $E_{nc1} = 3 \times 10^{10} \text{ Pa}$, $\epsilon_1 = 0.5$) serves as the filler materials for the longitudinal joint. Meanwhile, the constitutive model for rubber proposed by Zhou [55] is also shown.

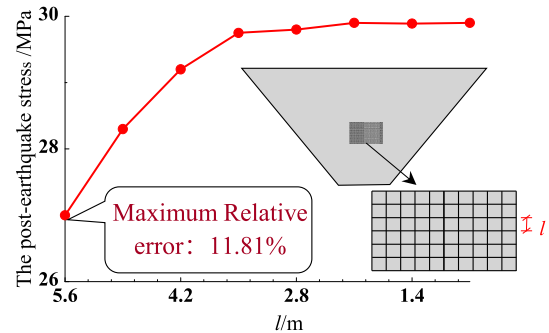


Fig. 22. Analysis of the size effect for the face slab along the slope direction.

Table 5

Error analysis for different sizes of elements along the slope direction.

Element size	5.6 m	4.9 m	4.2 m	3.5 m	2.8 m	2.1 m	1.4 m	0.7 m
Relative error/%	11.81	2.53	2.15	0.88	0.51	0.39	0.32	–

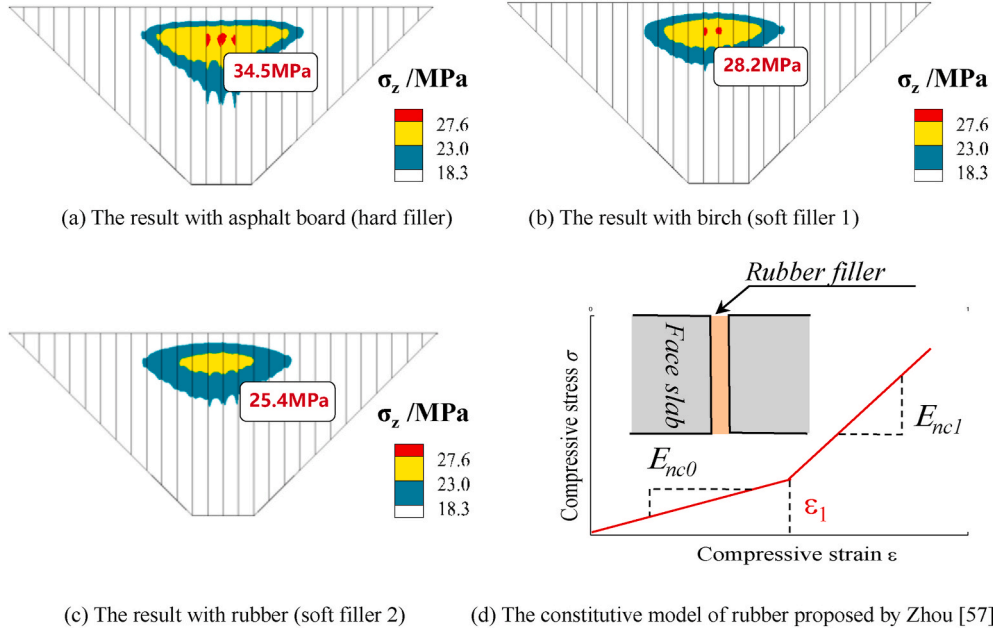


Fig. 23. Stress distributions for different filler materials used in longitudinal joint.

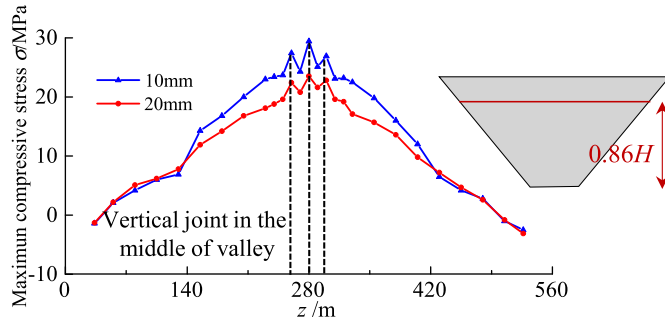


Fig. 24. The comparison of compressive stress with different width of longitudinal joint (asphalt boards).

As parts of extrusion displacement in the face slab along axial direction of the dam can be absorbed with soft filler, the maximum compressive stresses decrease by 19% and 26% in cases (b) and (c), respectively compared with the case of the hard joint. In addition, the area that exceeds the compressive strength of concrete decreased by 64% in case (b) or even disappeared in case (c). Thus, the axial compressive stress and extrusion damage can be effectively reduced by using soft joint materials.

(2) Increase the width of vertical joint

In this section, we conduct a study to verify whether the increase of vertical joint width can decrease the compressive stress along the dam axial direction. As mentioned above, the width of the vertical joint is 10 mm in case (a), and in this section, an additional case (d) with 20 mm vertical joint is introduced to conduct a dynamic analysis. The post-earthquake compressive stress of the outmost layer face slab at $0.86H$ level (the position of maximum compressive stress) is shown in Fig. 24.

The case (a) (10 mm for the joint) and case (d) (20 mm for the joint) have the same modulus for the filler material, but differ in the width of the joint, which can result in different stiffnesses. Thus, the decrease of compressive stress occurs in case (d), which has smaller stiffness. Meanwhile, the reduction in stress reached 20% in the middle of face slab, where the extrusion phenomenon is most serious. The compressive

stress is almost the same near the boundary of the face slab as the extrusion is not as significant.

5. The simulation of extrusion damage for face slab

The previous section evaluated the high compression zone of face slab under strong seismic load. The maximum post-earthquake compressive stress along the dam axial direction reached 29.4 MPa, which exceeds the uniaxial compression strength of C30 concrete (27.8 MPa) and can lead to extrusion damage. However, upon reaching the compression strength, the concrete starts to soften and cause stress redistribution. In addition, the uniaxial yield criterion is not suitable for three-dimensional face slabs. Therefore, the elastic model for concrete face slab may be misleading.

Thus, the concrete plastic damage model [56,57] is introduced to simulate extrusion damage for the face slab. D represents the value of stiffness degradation, which can be used to evaluate the degree of concrete damage based on the incremental theory of plasticity (0 for intact and 1 for completely damaged). The constitutive model considered the stiffness softening for concrete can be expressed in following equation:

$$\sigma = (1 - D)\bar{\sigma} = (1 - D)E_0 : (\varepsilon - \varepsilon^p) \quad (38)$$

where $\bar{\sigma}$ represents effective stress, E_0 is the initial elastic modulus of concrete, and ε and ε^p are total strain and plastic strain, respectively.

The yield function containing the effective stress and damage degree is as follows:

$$F(\bar{\sigma}, \kappa) = \frac{1}{1 - \alpha} \left(\alpha \bar{I}_1 + \sqrt{3} \bar{J}_2 + \beta \langle \bar{\sigma}_{\max} \rangle \right) - c(\kappa) \quad (39)$$

where α and β are dimensionless parameters, $\langle \bar{\sigma}_{\max} \rangle$ is the representative value of the maximum principle stress, κ is the damage state variable, and c is the strength parameter. The parameters for concrete face slabs are listed in Table 6.

Table 6
Parameters of concrete plastic damage model [4].

$\rho/\text{kg/m}^3$	E/GPa	ν	f_t/MPa	f_c/MPa	$G_t/\text{N} \cdot \text{m}^{-1}$
2450	31	0.167	3.48	27.6	325

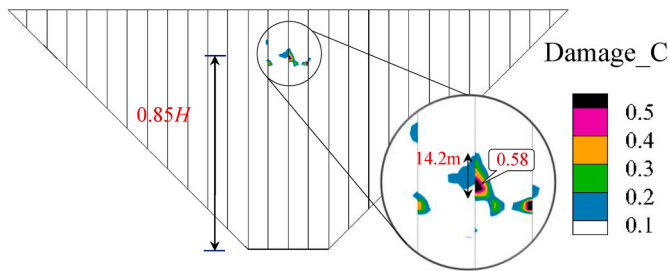


Fig. 25. The distribution of the post-earthquake extrusion damage for face slab.

In Table 6, f_c is compression strength, f_t is tensile strength, G_f is fracture energy (Note: this manuscript mainly focuses on the compression damage). The distribution of the post-earthquake extrusion damage for face slab is illustrated in Fig. 25.

The results show that the maximum damage factor can reach 0.58 at a height of $0.85H$. The maximum damage factor also lies near the vertical joint in the middle of the valley (about 14 m along the slop direction). In addition, the extrusion damage zone of the face slab with plastic damage constitutive model is not completely the same as the high compression zone with elastic model (i.e. exceeds the uniaxial compression strength). As mentioned above, the concrete face slab starts to soften and cause stress redistribution upon reaching the compression strength, and the uniaxial yield criterion is not suitable for modeling three-dimensional face slabs. Thus, the plastic damage constitutive model for the face slab can simulate extrusion damage under strong seismic load more accurately. It should be noted that both the linear model and the plastic damage model can reflect the characteristics of the extrusion damage locally within the superficial zone of the face slab.

6. Conclusion

It is difficult to use any single numerical method to simulate the high compressive zone and extrusion damage problems with high precision in CFRDs. Thus, this manuscript leverages a collaborative effort between SBFEM, non-matching node interfaces and non-conforming elements to establish a 3D cross-scale model for a typical 240 m high CFRD. Meanwhile, a simulation using a generalized plasticity model, a generalized plastic interface model and a plastic damage model is conducted to investigate the characteristics of the high compressive zone and the behavior of extrusion phenomenon under strong seismic loads. Through the above numerical simulation, several conclusions can be summarized as follows:

- (1) Combined loads of self-, weight, water pressure, friction forces and seismic load, the rockfill zone and consequently the concrete face slab to deform. Due to restriction of bedrock and the relative thinness across the entire face slab, bending and rotating may occur near the longitudinal joints. Thus, stress concentration occurs at the surface of face slab, which leads to the occurrence of a high compressive zone.
- (2) The post-earthquake high compressive zone along dam axial direction is located around a height of $0.85H$ within the surface of face slab and is situated in the middle of the valley near the vertical joints.
- (3) To model the process of high compressive stress, the meshes comprising the face slab must be refined adequately. Results generated from coarse meshes along the axial direction and thickness direction can underestimate the compressive stresses by up to 40% and 30%, respectively. However, the mesh along the slope direction is minimally affected.
- (4) Replacing hard joints with soft materials and increasing the width of the vertical joint are two effective methods to reduce the high compressive zone. Both approaches can decrease the stiffness of

the vertical joint in the dam axial direction and absorb a part of the extrusion displacement. The approaches reduced the maximum compressive stress by about 25% and 20% in the simulation presented in this manuscript.

- (5) Both the elastic model and plastic damage model of the face slab can reflect the characteristics of extrusion damage locally within the superficial zone of the face slab. By considering the softening of stiffness and the three-dimensional yielding criterion, the plastic damage constitutive model for the face slab can simulate extrusion damage under strong seismic loads more accurately.

This manuscript identifies the high compressive zone and simulates the extrusion damage of a face slab under strong seismic loads. The findings of this manuscript can provide an effective evaluation strategy for designing the ultimate aseismic capacity in high CFRDs. In addition, the presented numerical algorithms can be encapsulated into a “super element” class, which facilitates implementation into commercial FEM platforms (e.g. ANSYS, Abaqus, etc.). The mechanisms and causes of extrusion damage in practical projects will undoubtedly be more complex due to factors such as irregular valleys, complex material partitions, creep and wetting deformation, etc. Meanwhile, the more advanced concrete constitutive model (i.e. rate-dependent constitutive model, etc.) forms the basis for further simulating extrusion damage of the face slab. Thus, future work should explore the mechanisms of extrusion damage and explain failure pathways with practical examples of high CFRDs using a more advanced concrete constitutive model.

Author statement

Jin Gong: Conceptualization, Methodology, Software. Degao Zou: Software, Validation. Xianjing Kong: Conceptualization, Resources. Jingmao Liu: Supervision. Kai Chen: Writing- Reviewing and Editing.

Declaration of competing interest

We declare that we have no financial and personal relationships with other people or organizations that can inappropriately influence our work, there is no professional or other personal interest of any nature or kind in any product, service and/or company that could be construed as influencing the position presented in, or the review of, the manuscript.

Acknowledgements

This work was supported by the National Natural Science Foundation of China (Grant Nos. U1965206, 51779034). The writers would like to greatly acknowledge all the financial support and express their sincerest gratitude.

References

- [1] Zou Degao, Zhou Yang, Ling Hoe I, et al. Dislocation of face-slabs of Zipingpu concrete face rockfill dam during Wenchuan earthquake. *J Earthquake Tsunami* 2012;6(2):1–17.
- [2] Arrau L, Ibarra I, Noguera G. Performance of Cogoti dam under seismic loading// *Concrete face rockfill dams—design, construction, and performance*. ASCE 1985: 1–14.
- [3] Saberi M, Annan CD, Konrad JM. Seismic response analysis of face slabs in concrete face rockfill dams. *J Earthq Eng* 2019;1–29.
- [4] Xu B, Zou D, Kong X, et al. Dynamic damage evaluation on the slabs of the concrete faced rockfill dam with the plastic-damage model. *Comput Geotech* 2015;65: 258–65.
- [5] Qu Y, Zou D, Kong X, et al. Seismic cracking evolution for anti-seepage face slabs in concrete faced rockfill dams based on cohesive zone model in explicit SBFEM-FEM frame. *Soil Dynam Earthq Eng* 2020;133.
- [6] Kim YS, Kim BT. Prediction of relative crest settlement of concrete-faced rockfill dams analyzed using an artificial neural network model. *Comput Geotech* 2008;35 (3):313–22.
- [7] Zhang Y, Kong X, Zou D, et al. Tensile stress responses of CFRD face slabs during earthquake excitation and mitigation measures. *Int J GeoMech* 2017;17(12): 04017120.

- [8] Liu J, Liu F, Kong X, et al. Large-scale shaking table model tests on seismically induced failure of Concrete-Faced Rockfill Dams. *Soil Dynam Earthq Eng* 2016;82: 11–23.
- [9] Liu J, Liu F, Kong X, et al. Large-scale shaking table model tests of aseismic measures for concrete faced rock-fill dams. *Soil Dynam Earthq Eng* 2014;61–62(3): 152–63.
- [10] Chen K, Zou DG, Tong HX, et al. Scaled boundary polygon formula for Cosserat continuum and its verification. *Eng Anal Bound Elem* 2021;126:136–50.
- [11] Zou DG, Chen K, Kong XJ, et al. An approach integrating BIM, octree and FEM-SBFEM for highly efficient modeling and seismic damage analysis of building structures. *Eng Anal Bound Elem* 2019;104:332–46.
- [12] Gong J, Zou DG, Kong XJ, et al. An extended meshless method for 3D interface simulating soil-structure interaction with flexibly distributed nodes. *Soil Dynam Earthq Eng* 2019;125.
- [13] Gong J, Zou DG, Kong XJ, et al. A non-matching nodes interface model with radial interpolation function for simulating 2D soil–structure interface behaviors. *Int J Comput Methods* 2020;12:2050023.
- [14] Dakoulas P. Longitudinal vibrations of tall concrete faced rockfill dams in narrow canyons. *Soil Dynam Earthq Eng* 2012;41:44–58.
- [15] Arici Y. Investigation of the cracking of CFRD face plates. *Comput Geotech* 2011;38 (7):905–16.
- [16] Xu Z. Research progresses and key technologies of CFRD construction. *J Hydraul Eng* 2019;50(1):62–74 [in Chinese].
- [17] Zhou MZ, Zhang BY, Zhang ZL, et al. Mechanisms and simulation methods for extrusion damage of concrete faces of high concrete-faced rockfill dams. *Chin J Geotech Eng* 2015;37(8):1426–32 [in Chinese].
- [18] Zhong H. Large-scale numerical simulation for damage prediction of high arch dams subjected to earthquake shocks [D]. PhD thesis. China: Dalian University of Technology; 2008.
- [19] Desai CS, Ma Y. Modelling of joints and interfaces using the disturbed-state concept. *Int J Numer Anal Methods GeoMech* 1992;16(9):623–53.
- [20] Chen K, Zou DG, Kong XJ. A nonlinear approach for the three-dimensional polyhedron scaled boundary finite element method and its verification using Koyna gravity dam. *Soil Dynam Earthq Eng* 2017;96:1–12.
- [21] Chen K, Zou DG, Tang HX, et al. Scaled boundary polygon formula for Cosserat continuum and its verification. *Eng Anal Bound Elem* 2021;126:136–50.
- [22] Yerry MA, Shephard MS. Automatic three-dimensional mesh generation by the modified-octree technique. *Int J Numer Methods Eng* 1984;20(11):1965–90.
- [23] Shephard MS, Georges MK. Automatic three-dimensional mesh generation by the finite octree technique. *Int J Numer Methods Eng* 1991;32(4):709–49.
- [24] Wilson EL, Taylor RL, Doherty WP, et al. Incompatible displacement models[M]// Numerical and computer methods in structural mechanics. 1973.
- [25] Wanji C, Cheung YK. The nonconforming element method and refined hybrid element method for axisymmetric solid. *Int J Numer Methods Eng* 2015;39(15): 2509–29.
- [26] Shi DY, Mao SP, Chen SC. An anisotropic nonconforming finite element with some superconvergence results. *J Comput Math* 2005;23(3):261.
- [27] Pastor M, Zienkiewicz OC, Leung KH. Simple model for transient soil loading in earthquake analysis. II. Non-associative models for sands. *Int J Numer Anal Methods GeoMech* 1985;9:477–98.
- [28] Zou DG, Xu B, Kong XJ, et al. Numerical simulation of the seismic response of the Zipingpu concrete face rockfill dam during the Wenchuan earthquake based on a generalized plasticity model. *Comput Geotech* 2013;49:111–22.
- [29] Liu J, Zou D, Kong X. A three-dimensional state-dependent model of soil – structure interface for monotonic and cyclic loadings. *Comput Geotech* 2014;61:166–77.
- [30] Liu H, Song E, Ling HI. Constitutive modeling of soil-structure interface through the concept of critical state Soil mechanics. *Mech Res Commun* 2006;33:515–31.
- [31] Yu X, Kong X, Zou D, et al. Linear elastic and plastic-damage analyses of a concrete cut-off wall constructed in deep overburden. *Comput Geotech* 2015;69(sep): 462–73.
- [32] Wolf JP, Song C. The scaled boundary finite-element method—a fundamental solution-less boundary-element method. *Comput Methods Appl Mech Eng* 2001; 190:5551–68.
- [33] Liu J, Zhang PC, Lin G, et al. High order solutions for the magneto-electro-elastic plate with non-uniform materials. *Int J Mech Sci* 2016;115:532–51.
- [34] Liu J, Hao CK, Ye WB, et al. Free vibration and transient dynamic response of functionally graded sandwich plates with power-law nonhomogeneity by the scaled boundary finite element method. *Comput Methods Appl Mech Eng* 2021; 376:113665.
- [35] Liu J, Zhang PC, Lin G, et al. High order solutions for the magneto-electro-elastic plate with non-uniform materials. *Int J Mech Sci* 2016;115:532–51.
- [36] Ooi ET, Song C, Tin-Loi F. A scaled boundary polygon formulation for elasto-plastic analyses. *Comput Methods Appl Mech Eng* 2014;268:905–37.
- [37] Ooi ET, Shi MG, Song CM, et al. Dynamic crack propagation simulation with scaled boundary polygon elements and automatic remeshing technique. *Eng Fract Mech* 2013;106:1–21.
- [38] Floater MS, Kós G, Reimers M. Mean value coordinates in 3D. *Comput Aided Geomet Des* 2005;22(7):623–31.
- [39] Liu GR, Gu YT. Comparisons of two meshfree local point interpolation methods for structural analyses. *Comput Mech* 2002;29:107–21.
- [40] Bui TQ, Khosravifard A, Zhang C, et al. Dynamic analysis of sandwich beams with functionally graded core using a truly meshfree radial point interpolation method. *Eng Struct* 2013;47:90–104.
- [41] Liu GR, Gu YT. Coupling element free Galerkin and hybrid boundary element methods using modified variational formulation. *Comput Mech* 2000;26:166–73.
- [42] Noroozi AR, Malekzadeh P, Dimitri R, et al. Meshfree radial point interpolation method for the vibration and buckling analysis of FG-GPLRC perforated plates under an in-plane loading. *Eng Struct* 2020;221(111000):1–20.
- [43] Belytschko T, Gu L, Lu Y. Fracture and crack growth by element free Galerkin methods. *Model Simulat Mater Sci Eng* 1994;115:277–86.
- [44] Su X, Yang Z, Liu G. Finite element modelling of complex 3D static and dynamic crack propagation by embedding cohesive elements in Abaqus. *Acta Mech Solida Sin* 2010;23(3):271–82.
- [45] Jie Y, Tang XW, Luan MT, Yang Q. Adaptive element free Galerkin method to analysis of earthquake induced liquefaction. *Earthq Eng Eng Vib* 2008;7(2): 217–24.
- [46] Hu Y, Zhang G, Cheng S, et al. Effect of vertical joints on stress-deformation behavior of CFRD. *Rock Soil Mech* 2009;4(4):1089–94 [in Chinese].
- [47] Liu JB, Lu YD. A direct method for analysis OF dynamic soil-structure interaction. *China Civ Eng J* 1998;31(3):55–64.
- [48] Newmark NM. A method of computation for structural dynamics. American Society of Civil Engineers; 1959.
- [49] Yoshida N, Kobayashi S, Suetomi I, et al. Equivalent linear method considering frequency dependent characteristics of stiffness and damping. *Soil Dynam Earthq Eng* 2002;22(3):205–22.
- [50] Zou Degao, Zhou Yang, Ling Hoe I, et al. Dislocation of face-slabs of Zipingpu concrete face rockfill dam during Wenchuan earthquake. *J Earthquake Tsunami* 2012;6(2):1–17.
- [51] Zhou MZ, Zhang BY, Jie YX. Numerical simulation of soft longitudinal joints in concrete-faced rockfill dam. *Soils Found* 2016;56(3):379–90.
- [52] Cao KM, Zhang ZL. Performance of the Tianshengqiao1 CFRD. *Int J Hydropower Dams* 2001;8(5):78–83.
- [53] Johannesson P, Tohlang SL. Lessons learned from mohale. *Int Water Power Dam Constr* 2007;59(8):16–25.
- [54] Arici Y. Investigation of the cracking of CFRD face plates. *Comput Geotech* 2001;38 (7):905–16.
- [55] Zhou MZ, Zhang BY, Jie YX. Numerical simulation of soft longitudinal joints in concrete-faced rockfill dam. *Soils Found* 2016;56(3):379–90.
- [56] Lubliner J, Oliver J, Oller S, Onate E. A plastic-damage model for concrete. *Int J Solid Struct* 1989;25:299–326.
- [57] Lee J, Fenves GL. Plastic-damage model for cyclic loading of concrete structures. *J Eng Mech* 1998;124(8):892–900.